Chapter 1:

Brain Tumor Detection and Segmentation: A Review of Optical Scanning Holography Method using Active Contour

Abdelaziz Essadike, Anass Cherkaoui, Abdennacer El-Ouarzadi, Abdenbi Bouzid

1. INTRODUCTION

A brain tumor is a mass of abnormal cells engaged in a chaotic process of driver somatic mutations [1], where they cause various symptoms, increasing the risk of damaging the brain. Indeed, the secondary tumor infiltrates neighboring healthy tissues and proliferates within the brain or its membranes, making it crucial to determine its shape and volume to ensure effective management of patients at an early stage of cancer. Magnetic resonance imaging (MRI) is the most commonly used non-invasive imaging modality for brain tumor detection [2]. MRI employs radio waves and a strong magnetic field to acquire a set of cross-sectional brain images. In other words, the 3D anatomical details of a tumor are presented as a set of parallel 2D cross-sectional images. Representing 3D data as projected 2D sections results in information loss and can raise questions about tumor prognosis. Furthermore, 2D cross-sectional images do not accurately represent the complexities of brain anatomy. Therefore, interpreting 2D images requires specialized training. This is why the reconstruction of volumes from sequential parallel 2D cross-sectional slices is a necessity for 3D visualization of tumors [3].

The 3D reconstruction of tumors initially requires appropriate segmentation of the region of interest. This 3D reconstruction helps radiologists better diagnose patients and subsequently eradicate the entire tumor when surgical intervention is considered. Techniques presented in [4,5] are based on preprocessing, image enhancement, and contouring before reconstruction. In 2012, authors in [6] utilized a technique based on phase contrast projection tomography to calculate the 3D density distribution in bacterial cells. In 2013, authors in [3] proposed an improved interpolation technique to estimate missing inter-slices, and the Marching Cubes (MC) algorithm for meshing the tumor. For

surface rendering, they applied the Phong shading and lighting model to better calculate the tumor's volume. Furthermore, an approach in [7], in 2019, offers a technique for segmenting brain tumors throughout the 3D volume using a 2D convolutional neural network to predict tumors. Authors in [8] conducted a comparison between conventional machine learning-based techniques and deep learning-based techniques. The latter are further categorized into 2D-CNN and 3D-CNN techniques. However, the results of techniques based on deep convolutional neural networks outperform those of machine learning techniques. As for authors in [9], they introduced a two-stage optimal mass transport technique (TSOMT) that involves transforming an irregular 3D brain image into a cube with minimal deformation for segmenting medical 3D images. Automatic segmentation, facilitated by convolutional neural networks, of a brain tumor from two-dimensional slices (coronal, sagittal, and axial) [10], significantly aids in delineating the region of interest in 3D.

Conventional holography, as we know it today, owes its inception to Hungarian-British physicist Dennis Gabor in 1948 [11]. His groundbreaking research aimed at enhancing the resolution of electron microscopes paved the way for this revolutionary technique. In the 1960s, with the emergence of lasers, holography saw significant development. Holograms were originally recorded on plates or photosensitive films, primarily relying on silver ions that darkened when exposed to light. The advent of high-resolution matrix detectors in 1994, championed by U. Schnars and W. Jüptner [12], heralded the era of digital holography. This development opened doors to a multitude of applications, including holographic microscopy [13,14], quantitative phase imaging [15-18], color holography [19-21], metrology [22-24], holographic cameras [25], 3D displays [26-28], and head-up displays [29,30]. An innovative breakthrough came with the introduction of phase-shifting holography by Yamaguchi and Zhang [31], aiming to eliminate unwanted diffraction orders from holograms. They employed spatial phase shifting using a piezoelectric transducer with a mounted mirror, and minor frequency adjustments of acousto-optic modulators (AOM), a technique closely related to heterodyne detection methods. Optical Scanning Holography (OSH) stands out as an intelligent application for processing pupillary interaction [32-35]. In 1979, Korpel and Poon introduced optical heterodyne scanning to implement the pupillary interaction scheme, while in 1992, Indebetouw and Poon innovated by incorporating this scheme into a scanning illumination mode. A pivotal moment occurred in 1985 [36] when Poon, through a clever adjustment of one lens relative to another (one serving as an open mask and the other as a pinhole mask), and by deliberately defocusing the optical system, developed an optical scanning system capable of holographically recording scanned objects. This ingenious technique marked the birth of optical scanning holography (OSH), which has since found diverse applications, including optical scanning microscopy, 3D shape recognition, 3D holographic TV, 3D optical remote sensing, and more. OSH's early forays into preprocessing can be traced back to 1985 [37]. Subsequent research indicated that replacing a flat lens with a Gaussian annular aperture was beneficial for recovering the edges of cross-sectional images in holograms [38]. In 2010, Xin Zhang and Edmund Y. Lam [39] showcased the efficiency of selecting a pupil function such as the Laplacian of Gaussian for extracting the edges of 3D scanned objects using the OSH system. Furthermore, authors in reference [40]

proposed a 1D image capture system for autostereoscopic displays, comprising a cylindrical lens, a focusing lens, and an imaging device. By scanning an object across a wide angle, they successfully synthesized 3D stereoscopic images, adding a unique dimension to the OSH technology landscape.

Progress in Optical Scanning Holography (OSH) represents a significant leap in the field of medical imaging and tumor detection. This progress is achieved through the strategic integration of innovative features and techniques that collectively enhance the capabilities of the method. One pivotal enhancement is the combination of off-axis optical scanning with a heterodyne fringe pattern [41-44]. This combination significantly improves the accuracy of tissue imaging. Off-axis scanning, which involves capturing data from multiple angles, allows for more precise 3D structure reconstruction. The heterodyne fringe pattern plays a crucial role in phase retrieval, making it easier to extract valuable information from the holographic data. The introduction of a Spatial Light Modulator (SLM) for MRI image display is another significant innovation. This technology enables the direct correlation of holographic data with anatomical MRI images, enhancing the precision of tissue visualization. By fusing the holographic and MRI data, this feature provides a more comprehensive and informative representation of the biological tissues under examination. Moreover, there is a dedicated focus on extracting the in-phase component of the scanned data. This precise component is essential for accurate tumor localization. The peak of the in-phase component serves as a reliable indicator of the tumor's position, reducing the likelihood of false positives and false negatives in diagnostic assessments [45,46]. Generalized Optical Scanning Holography (GOSH) represents a significant leap in data collection efficiency. GOSH can acquire a single on-axis hologram, significantly expediting the process while minimizing the risk of motion artifacts. This is particularly advantageous for 3D imaging, where efficiency is paramount. Furthermore, the method incorporates a cylindrical lens for line-by-line scanning, enhancing the speed and accuracy of data collection [47] . This approach contributes to more efficient data acquisition, reducing the time required for the scan while enriching the dataset. The utilization of an Active Contour Model (ACM) for segmentation is another crucial addition. ACMs are efficient in delineating complex shapes and contours, making them well-suited for identifying abnormal tissue regions [48]. By automating the segmentation process and incorporating the tumor's position, the method ensures that the area of interest is precisely encompassed. Transitioning active contour theory from semi-automatic to fully automatic status with reliable tumor detection, our method's effectiveness is demonstrated through tests using the well-known BraTS 2019 and BraTS 2020 databases. Ultimately, the goal of this methodology is to reconstruct 3D brain tumors from segmented areas of interest, offering a comprehensive view of tumor size and location. These added features and enhancements are of utmost significance, as they collectively contribute to faster, more accurate, and more informative assessments of biological tissues. By enabling early and precise tumor detection, this methodology holds the potential to significantly improve patient outcomes, making it a valuable asset in the realm of medical diagnostics and research.

2. MATERIALS AND METHODS

2.1 The First Iteration: Off-Axis Optical Scanning Holography

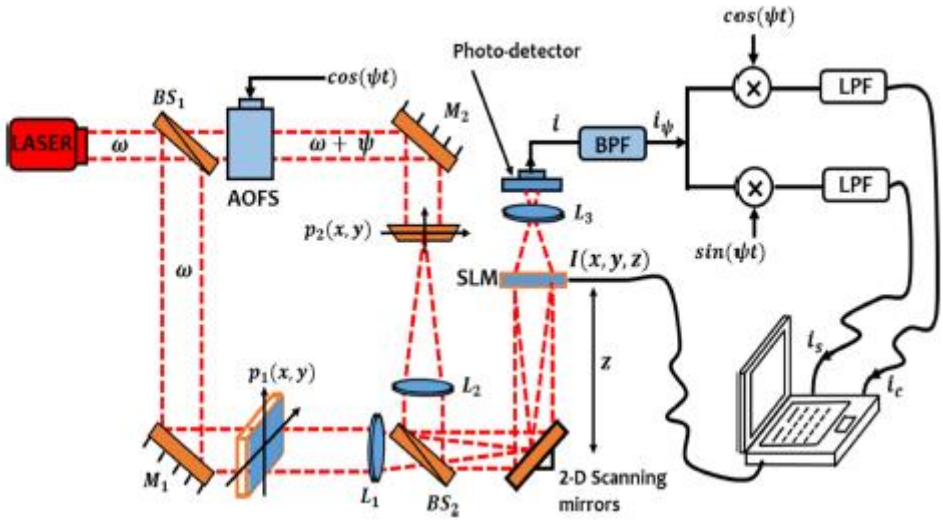

Figure 1: Two-pupil optical heterodyne scanning image processor for the in-phase component extraction of brain tumor.

Figure 1 illustrates the Optical Spatial Heterodyne (OSH) system used for the extraction of the in-phase and quadrature components of scanned current information. The system configuration is as follows: A laser source emits light with temporal frequencies ω. This light is split into two beams using a Beam Splitter BS_1, and the laser source in use operates at two wavelengths, $532\ nm$ and $1064\ nm$. The first beam, following reflection from Mirror M_1, illuminates the first pupil, designated as $p(x,y)$. In contrast, the second beam undergoes a frequency shift through an acousto-optic modulator. After reflecting off Mirror M_2, the frequency of the laser illuminating the second pupil, $p(x,y)$, becomes $(\omega + \psi)$. Both pupils are then combined using Beam Splitter BS_2, focusing the light onto $2D$ scanning mirrors located at the rear focal plane of Lenses L_1. These optical beams are further directed to a Spatial Light Modulator (SLM), which imparts spatially varying modulation based on MRI data onto the light. The SLM used here is known as LC 2012, featuring a resolution of 1024 x 768 pixels. This SLM is responsible for displaying the brain tumor image, denoted as $I(x,y,z)$, located at a specific distance z from the $2D$ scanning mirrors. It's not worthy that SLMs have historically encountered issues related to diffraction efficiency because of phase shift limitations. However, the selected SLM effectively overcomes this challenge. It can achieve a phase shift range approaching 2π, resulting in significantly enhanced diffraction efficiency. Furthermore, the LC 2012 SLM offers the capability to modulate the blazing function, thereby improving grating efficiency and overall diffraction performance. The system is completed by Lens L_3, which focuses transmitted light onto a photo-detector, producing an output current, $i(x,y)$. An electronic bandpass filter (BPF), tuned to the heterodyne frequency ψ, provides an output of a swept current, denoted as $i_{\psi}(x,y)$.

$$i_{\psi_Q}(x,y,z+z_0) = P^1_{z+z_0}\left(\frac{k_0 x'}{f},\frac{k_0 y'}{f}\right) P^{2\,*}_{z+z_0}\left(\frac{k_0 x'}{f},\frac{k_0 y'}{f}\right) \otimes |O(x,y,z+z_0)|^2 \quad (1)$$

Afterward, we are able to define the optical transfer function (OTF) of the system by:

$$OTF_{\Psi}(k_x,k_y,z+z_0) = \frac{F\left\{i_{\psi_Q}(x,y,z+z_0)\right\}}{F\{|O(x,y,z+z_0)|^2\}} \quad (2)$$

As a result, we obtain the following equations:

$$\mathrm{i_c(x,y)} = \mathrm{Re}\left\{\int \mathrm{F^{-1}\{F\{|O(x,y,z+z_0)|^2\}.OTF_{\Psi}\}\,dz}\right\} \quad (3)$$

$$\mathrm{i_s(x,y)} = \mathrm{Im}\left\{\int \mathrm{F^{-1}\{F\{|O(x,y,z+z_0)|^2\}.OTF_{\Psi}\}\,dz}\right\} \quad (4)$$

These two currents are respectively representing the In-phase component $\mathrm{i_c(x,y)}$ and the quadrature component $\mathrm{i_s(x,y)}$ of the extracted heterodyne current from the scanned MR image. the temporal frequency shift is inserted between the two pupils by assuming

$P^1_{z+z0}\,(x,y)$ = 1 and $P^2_{z+z0}\,(x,y)$ = $\delta(x,y)$ Thus, the optical transfer function becomes:

$$\mathrm{OTF_{\Psi}(k_x,k_y,z+z_0)} = \exp\left[\frac{-j(z+z_0)}{2k_0}\left(k_x{}^2+k_y{}^2\right)\right] \quad (5)$$

and the two streams become:

$$\mathrm{i_c(x,y)} = \int\left\{|O(x,y,z+z_0)|^2 * \frac{k_0}{2\pi(z+z_0)}\sin\left[\frac{k_0}{2(z+z_0)}(x^2+y^2)\right]\right\}dz \quad (6)$$

$$i_s(x,y) = \int\left\{|O(x,y,z+z_0)|^2 * \frac{k_0}{2\pi(z+z_0)}cos\left[\frac{k_0}{2(z+z_0)}(x^2+y^2)\right]\right\}dz \quad (7)$$

2.2 The Second Iteration: In-Line Optical Scanning Holography

In the progression of our Optical Scanning Holography (OSH) setup, the transition from the off-axis holography structure to inline holography marked a pivotal shift in our methodology. Off-axis holography, characterized by a physical separation of the object and reference beams at an angle, was succeeded by inline holography, where these beams are aligned. This alteration bears significant implications. Off-axis holography excels in extracting precise phase information, and its sensitivity to phase variations is conducive to accurate $3D$ reconstruction. However, it can be susceptible to speckle noise and is more sensitive to vibrations. In contrast, inline holography simplifies the optical setup, supports real-time imaging, and offers a more streamlined approach, significantly enhancing the speed of data acquisition. By virtue of its direct correlation of holographic and MR image data through the spatial light modulator (SLM), inline holography enhances the accuracy of tissue visualization, a fundamental feature for our diagnostic objectives. This transition has not only expedited data acquisition but also ensured greater precision and efficiency in our holographic imaging, setting the stage for subsequent enhancements.

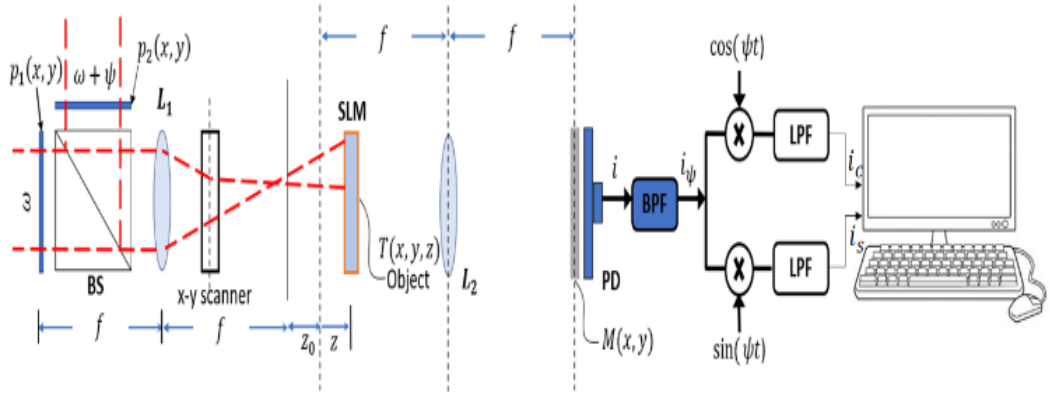

Figure 2:Generalized two-pupil heterodyne scanning image processing system for the In-phase component extraction of brain tumor.

In this section, we present the transition to an inline holography setup for our imaging process, departing from the previous off-axis configuration. Our primary focus is on the automatic detection of tumors, utilizing the In-phase component of the scanned current. To maintain this crucial component during data acquisition, we adopt a novel optical heterodyne approach. For instance, we implement acousto-optic modulators to manipulate the laser beam frequency. The heart of our inline holography system involves the merging of two laser beams through a beam splitter (BS). These combined beams are directed by an $x-y$ scanner towards a $3D$ object positioned at a distance of $z+z_0$ from the back focal plane of lens L_1. This object is placed within a spatial light modulator, which plays a pivotal role in our holographic imaging process. Each slice of the object is represented by an amplitude transmittance $T(x,y,z)$, and the spatial light modulator displays the brain tumor image, labeled as $I(x,y,z)$, situated at a distance of $z+z_0$ away from the back focal plane of lens L_1. Moreover, as we transition to this inline setup, we encounter challenges related to diffraction efficiency, particularly associated with phase shift loss.

This transition is essential because the MRI image is binary, and our chosen spatial light modulator can effectively achieve an offset range of nearly 2π, resulting in exceptional diffraction efficiency. Additionally, the spatial light modulator stands out as a modern device, allowing us to modulate blazing functions to attain maximum grating efficiency and significantly enhance diffraction performance. These adjustments are critical in our pursuit of precise holographic imaging.

In the context of our study, we define the in-phase component, $i_c(x, y)$, and the quadrature component, $i_s(x, y)$, of the extracted heterodyne current from the scanned MR image as follows:

$$i_c = \int \left\{ |T(x, y; z)|^2 * \frac{k_0}{2\pi z} sin \left[\frac{k_0(x^2+y^2)}{2z} \right] \right\} dz = H_{\sin(s,y)} \quad (8)$$

$$i_s = \int \left\{ |T(x, y; z)|^2 * \frac{k_0}{2\pi z} cos \left[\frac{k_0(x^2+y^2)}{2z} \right] \right\} dz = H_{\cos(s,y)} \quad (9)$$

2.3 The Third Iteration: Cylindrical Lens-Integrated Optical Scanning Holography

To enhance the precision and efficiency of our approach, we leverage the invaluable benefits of cylindrical lens L_1 in the context of optical scanning holography for the automated segmentation of $3D$ brain tumors from MRI data. L_1 plays a pivotal role in optimizing our method in several ways. Firstly, it enables meticulous line-by-line scanning, which is crucial for capturing intricate details within the MRI images. The cylindrical lens L_1 configuration ensures that each section of the image is consistently and accurately scanned, reducing the likelihood of information loss or distortion. Secondly, the integration of cylindrical lens L_1 in our system enhances the depth perception and spatial accuracy of the captured data. By focusing on specific areas of interest within the MRI images, L_1 ensures that the relevant tumor structures are precisely imaged and analyzed. This level of precision not only accelerates the segmentation process but also reduces the risk of misinterpretation, which can occur in manual delineation. Moreover, cylindrical lens L_1 is instrumental in optimizing the digitization of the phase component of the scanned data. This digital representation is critical for pinpointing the exact location of the tumor within the brain, as the peak of the phase component reliably indicates its position. This information serves as the foundation for rapid segmentation and subsequent $3D$ tumor reconstruction. In summary, the inclusion of cylindrical lens L_1 in our approach significantly enhances the overall accuracy, speed, and reliability of tumor segmentation, making it an indispensable component in our quest to streamline neuroimaging and improve patient care. L_1 allows for a higher level of precision and detail, reducing the margin of error and contributing to the system's efficacy in advancing medical diagnostics and treatment planning.

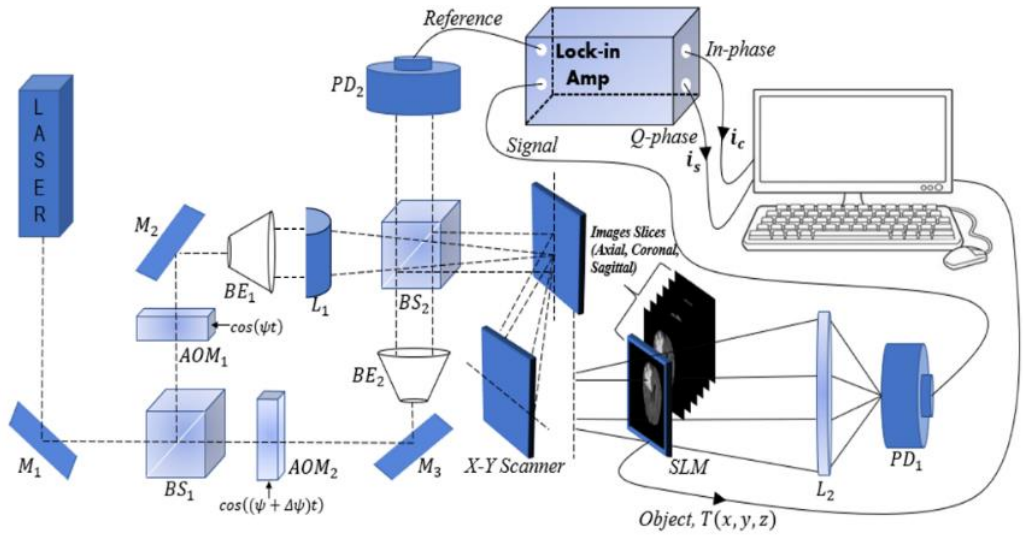

Figure 3: Schematic setup of the optical scanning holography (OSH).

Figure 1 displays the optical scanning holography system used for our method. A laser beam of frequency ω is shifted in frequency to ψ and $\psi + \Delta\psi$ through acousto-optic modulators ($AOM_{1,2}$), respectively. The beams from AOMs are then collimated by collimators BE_1 and BE2. The outgoing beam from BE_2 is considered a plane wave of frequency $\omega + \psi + \Delta\psi$, which is projected onto the object through the $x - y$ scanner. Our novel method involves integrating into the chosen imaging system a cylindrical lens L_1, which provides a cylindrical wave at $\omega + \psi$, projected onto the object. A focusing lens is also used to capture a large number of elemental images containing extensive parallax data. These elemental images are transformed into a matrix of elemental images, where each captured elemental image corresponds to a vertical line in the ray space [46]. The utilization of this linear scanning technology involves capturing object images in a single pass rather than point by point, while adjusting the shape of the surface after each iteration, resulting in computational time savings. Accordingly, following appropriate sampling for viewing conditions, we achieved fully automatic segmentation through the improved algorithm and the arrangement of color filters. This allowed the transformation of two-dimensional elemental images into three-dimensional ($3D$) images, as demonstrated in Figures 5 and 6.

The $x - y$ scanner is used to uniformly scan the $3D$ object, line by line. As a result, each scan line of the object corresponds to a line in the hologram at the same vertical position. Along each scan line, photodetectors PD_1 and PD_2 are employed to capture the optical signal scattered by the object and the heterodyne frequency information $\Delta\psi$ as a reference signal, respectively, and convert them into electrical signals for the lock-in amplifier. The in-phase and quadrature-phase outputs of the lock-in amplifier circuit produce a sine hologram, $H_{\sin(s,y)}$, and a cosine hologram, $H_{\cos(s,y)}$, to achieve a full $2D$ scan of the object, as illustrated below:

$$H(x,y) = H_{cos}(x,y) + jH_{sin}(x,y) = \sum_{k=0}^{N-1} H_k(x,y;\ z_k) \tag{10}$$

2.4 Core Principle of OSH

The central premise of our proposed approach centers on harnessing the In-phase component (denoted as $i_c(x,y)$) within MR images to discern abnormal tissue. In Figures 1,2 and 3, the optical system yields an output illustrating the distribution of the In-phase component via heterodyne current. We designate the prominent points in this output as "In-phase component peaks." Figure 4 furnishes visual illustrations of these In-phase component peaks, detected using the OSH method. Consequently, we can accurately locate brain tumors by identifying these peaks in the In-phase component distribution.

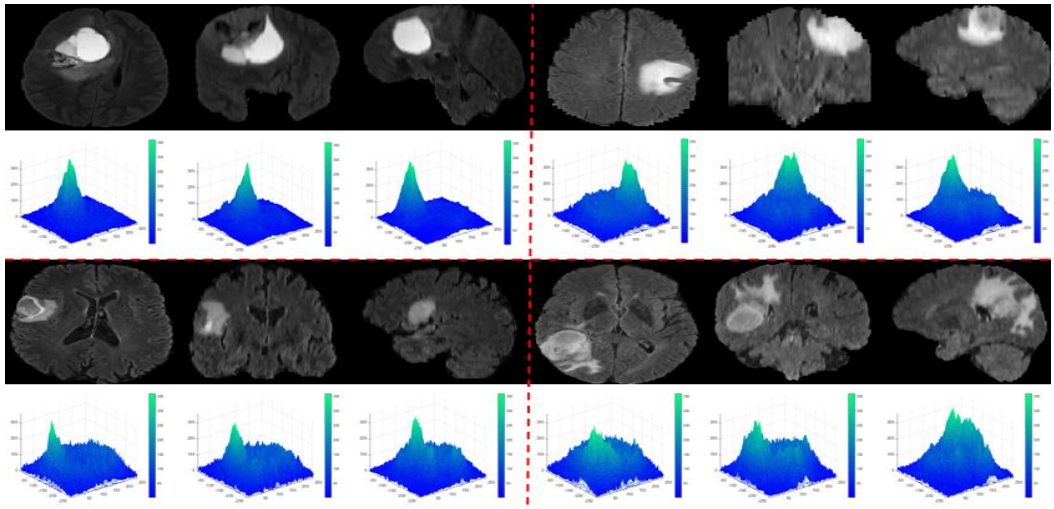

Figure 4: In-phase component peaks at the proposed OSH method's tumor position: examples of image slices (Axial, Coronal, Sagittal) from BRATS 2019 database.

Armed with knowledge about the positions of these In-phase component peaks, as depicted in Figure 5, we can establish the initial contour (C_i) for tumor segmentation within the affected tissue. This initial contour serves as a critical foundation for further analysis and refinement of the tumor's boundaries. Our proposed method is highly adaptable, capable of effectively detecting multimodal tumors by pinpointing the positions of two maxima within the In-phase component peaks. This feature proves invaluable in cases involving tumors with multiple characteristics or modalities, enhancing our ability to provide tailored and precise diagnoses and treatment strategies for patients facing complex tumors.

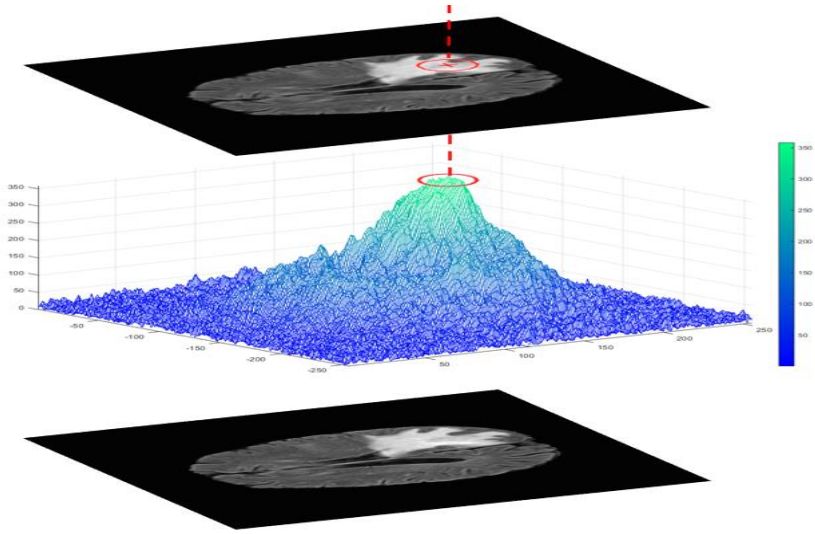

Figure 5: Preliminary extraction of the initial contour Ci inside the tumor tissue by OSH-based phase component peaks

3. RESULTS AND DISCUSSION

3.1 Evaluation of detection phase

Various methods are used to detect tumor contours, including derivative methods, which are based on evaluating the variation at each pixel by identifying maxima. determining the brain tumor's position by searching the peaks given by the maximum values of the In-phase component distribution. With the peaks position of the In-phase component, as shown in Figure 4, we extract the initial contour C_i of the tumor segmentation within the tumor tissue. The proposed method can be adapted to detect multimodal tumors by detecting the two maxima's two positions of the In-phase component peaks.

The output results of the OSH optical process are digitally implemented to extract the following parameters: c the center of the tumor, L the amplitude of the In-phase component peak, and C_i the initial contour formed using the principal in Figure 5. the suggested method detects tumor tissue and facilitates the energy calculation of active contours. Using the initially detected contour C_i, we calculate the averages of the image $I(x, y)$ inside C_i and outside C_i to define the active contour model:

$$\mathrm{E_{i,j}} = \alpha.\,\mathrm{C_{i,j}} + \beta.\left|\mathrm{I} - \mathrm{M_{i,j}}\right|^2 + \gamma.\left|\mathrm{I} - \mathrm{m_{i,j}}\right|^2 \qquad (11)$$

where: $\alpha = \beta = \gamma = 1$ are fixed parameters. $\mathrm{C_{i,j}}$ is the initial contour detected by the proposed method. $\mathrm{m_{i,j}}$ is the average of the input RM image $I(x, y)$ inside the initial contour $\mathrm{C_{i,j}}$. $\mathrm{M_{i,j}}$ is the average of the input RM image $I(x, y)$ outside the initial contour

$C_{i,j}$. Besides, the evolution of the initial contour detected by the OSH system is realized through the programming of the proposed active contour pattern, based on finite differences obtained after linearization and discretization of the equation energy (11).

In our system in figure 3, the phase component enables us to extract the phase current after line-by-line scanning of the object images, as shown in figure 4. The maximum values characterizing this output are called phase component peaks. Contours delimiting these peaks are drawn, creating the regions of interest within the tumor tissue.

As the decision of the existence of a brain tumor on an MR image is based on the parameter *L*, we have studied *L* values for MR images of healthy and tumor brains. Figure 5 represents the statistical distribution of the *L* parameter in the two cases mentioned. Evidently, in the case of the tumor, *L* values are large compared to the healthy brain. In the images of healthy brains, the average *L* in the images used was 110, and in the images of brain tumors was 325. It should be noted that the maximum peaks of In-phase components given by the OSH process, which localized the tumors, were within the margin of [300; 350]. This margin increases to over 255 due to the multiplication of the MRI images in equation 10. Moreover, due to the uniform distribution of pixel intensity in images of the healthy brain, all of the maximum peaks of the In-phase component in cases of healthy brains being within [100 ; 120]. Therefore, the parameter *L* given by the OSH process is a reliable parameter to decide the existence of a tumor in the MR images.

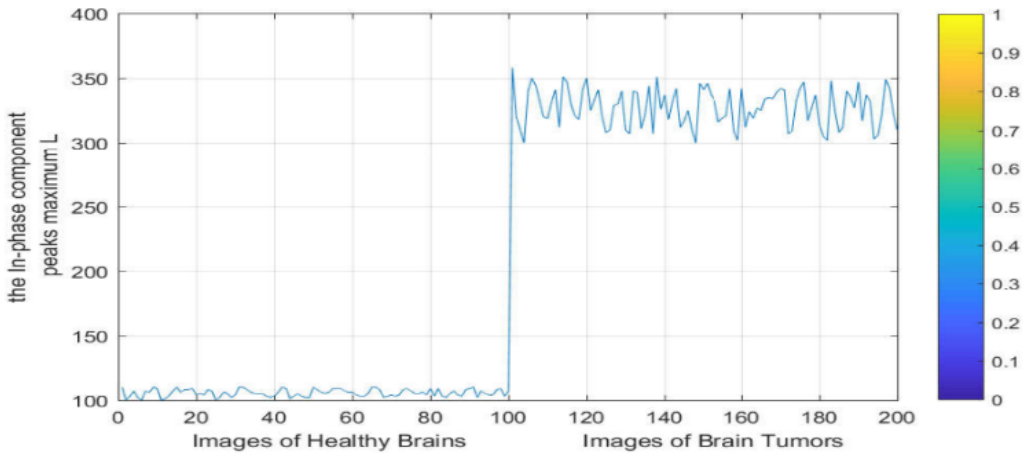

Figure 6: Distribution of the L parameter in the healthy and tumorous brain images.

Similarly, the brain tumor position's decision is based on the parameter *c* given by the OSH. Therefore, we have estimated the precision of the proposed method regarding the detection of *c* inside of the tumor tissue. As a comparison, we have also calculated the percentage rate of the potential field segmentation (PFS) algorithm in [49] regarding tumor centers' detection. This approach is founded on potential field analogy in detecting brain tumors by assuming the intensity of a pixel as a mass, creating a potential field. It

should be pointed out that the center used is obtained from the maximum peaks of the In-phase component. Table 1 reveals the high accuracy of detecting the center of the tumor tissue by the proposed method. In 98.5% of the patients (from both databases), the maximum peaks of In-phase components given by the proposed method are located in the tumor tissue center. In the remaining 1.5%, the OSH returned parameter c to the border of this tumor. Two principal reasons explain these results; firstly, owing to the modalities used in MR images to separate tumors from healthier tissue, contrast provides an almost unique signature for each type of tissue, particularly the type of tumor, which appears in most cases with the white color. Secondly, the high value of the maximum peaks of the In-phase component in tumoral regions. Therefore, the proposed method is a promising technique for detecting anomalous tissue in MR images, comparing with recently published methods. The proposed method is more accurate and quicker. It should be noted that the center used is determined by the maximum peak of the In-phase component.

Table 1: Percentage of the proposed method in terms of the c parameter return within the tumor tissue and the meantime, comparing to the method in [49].

Method	**Accuracy (%)**			**Time average (seconds)**
	Inside tumor	**Edge tumor**	**Outside tumor**	
Potential Field [29]	95%	0	5%	38.1643
Proposed method	98.5%	1.5%	0%	0.2009

3.2 Evaluation of segmentation phase

Following our previous works [41- 47], we explored the use of OSH in automatizing tumor tissue detection in MRI, enhanced framework for optical scanning holography (OSH) to detect abnormal tissue regions. We improve [41] in terms of acquisition speed, accuracy, and data size. In addition, the Generalized Optical Scanning Holography (GOSH) of recording holographic information is advantageous as on-axis holograms are acquired simultaneously, unlike standard phase-shifting holography where their holograms are acquired sequentially. To test the last proposed method in a very demanding way and link it to clinical imaging applications, we have used 20 images of patients with the most challenging segmentation conditions. These images contain different shapes, sizes, and contrasts of tumors, Tables 2 compare the performance reported from these 20 images and reached by the GOSH method with the Geodesic Active Contour model (GAC) [50], the Localized Active Contour (LAC) [51], the Active Contours by Cuckoo Search (ACCS) [52] and our previous work [41]. Compared to other ACMs, the proposed method performs better in terms of Sen, D, H, and Spe parameters. For evidence, the sensitivity value of 0.9961 reached by the proposed method was the

highest obtained, and its Hausdorff distance of 2.0000 was the lowest. Besides, its highest average specificity value of Spe = 1.0000 indicates that it can correctly classify healthy tissue more than other ACM-based methods. It should be noted that the highly efficient performance of all methods in terms of the Spe parameter is explained by the fact that all the initial contours detected by the proposed OSH technique are located inside the tumor tissue. Following these methods' development, the optimal segmentation contours remain inside the tumor tissue, making the FP parameter very close to zero. Also, it can be observed from Table 2 that our proposed method [47] reduces the calculation time (in seconds) Figure 7.

Table 2: Sensitivity, Dice, Hausdorff distance, Specificity, and elapsed time rates obtained from the optimal contour of the BRATS 2012 databases images reached by using the Geodesic Active Contour (GAC), the Localized Active Contour (LAC), the Active Contour driven by Cuckoo Search (ACCS), our previous work (OSH-ACM) and our proposed method (Proposed).

Patients	**Method**	Sen	D **(AVG±SDx 10^{-4})**	H_d	Spe	**Time (s)**
Patient 1 (BRATS 2012)	GAC	0.7194 ±1.2	0.7650±6.3	4.1200 ±2.6	0.9945±0.0	14.9945±1.2
	LAC	0.9016 ±2.6	0.9482±3.3	2.7488 ±2.6	0.9975±2.3	14.2406±1.9
	ACCS	0.9502 ±7.5	0.9495±9.0	2.6488 ±5.2	0.9980±1.0	48.1200±2.0
	OSH-ACM	0.9772 ±0.5	0.9838±0.3	2.0458 ±0.0	0.9987±4.5	0.2937±3.1
Patient 2 (BRATS 2012)	GAC	0.7844 ±0.0	0.7377 ±4.2	4.3589 ±6.1	0.9903 ±4.5	26.1737 ±2.5
	LAC	0.8250 ±5.4	0.9041 ±4.8	4.0010 ±2.0	0.9957 ±2.8	17.1943 ±9.5
	ACCS	0.9347 ±1.5	0.9605 ±0.8	3.0050 ±2.5	0.9989 ±1.1	46.9430 ±9.0
	OSH-ACM	0.9752 ±0.2	0.9753 ±0.1	2.1623 ±0.0	0.9980 ±0.0	0.3540 ±7.2
Patient 3 (BRATS 2012)	GAC	0.6804 ±6.3	0.7489 ±5.6	5.7823 ±2.4	0.9902 ±0.3	27.7494 ±2.8
	LAC	0.6715 ±2.3	0.8417 ±5.3	4.8990 ±7.5	0.9914 ±0.0	17.3898 ±7.0
	ACCS	0.9274 ±3.8	0.9410 ±4.1	3.5560 ±7.1	0.9992 ±0.9	59.2705 ±2.7
	OSH-ACM	0.9898 ±0.1	0.9897 ±0.1	2.0623 ±1.0	1.0000 ±0.1	0.2530 ±3.8

Patient 4 (BRATS 2012)	GAC	0.5751 ±3.7	0.6456 ±0.1	4.1231 ±8.7	0.9976 ±1.7	37.9528 ±8.7
	LAC	0.6346 ±2.0	0.7765 ±1.0	4.3589 ±5.7	0.9950 ±4.6	17.6072 ±8.0
	ACCS	0.8892 ±3.9	0.9395 ±1.0	3.3940 ±3.3	0.9989 ±7.4	25.7492 ±5.4
	OSH-ACM	0.9867 ±0.1	0.9834 ±0.1	2.0056 ±1.0	0.9997 ±0.7	0.2212 ±1.5
Patient 5 (BRATS 2012)	GAC	0.7247 ±3.4	0.6902 ±2.8	5.7958 ±3.9	0.9906 ±5.5	22.1867 ±9.6
	LAC	0.7678 ±2.0	0.7243 ±0.0	4.0001 ±1.0	0.9907 ±0.5	16.6965 ±0.8
	ACCS	0.9192 ±2.1	0.9380 ±0.2	3.5437 ±1.0	0.9984 ±6.6	18.4792 ±0.8
	OSH-ACM	0.9894 ±0.2	0.9757 ±0.1	2.5826 ±1.0	0.9997 ±4.4	0.2165 ±2.6
Patient 6 (BRATS 2012)	GAC	0.7800 ±5.4	0.8096 ±1.7	3.0010 ±2.0	0.9950 ±2.2	9.3899 ±7.4
	LAC	0.7473 ±0.3	0.7181 ±0.1	3.0000 ±0.0	0.9975 ±7.9	10.5313 ±0.9
	ACCS	0.9247 ±2.0	0.9400 ±2.3	2.8947 ±9.7	0.9998 ±2.3	15.3692 ±5.0
	OSH-ACM	0.9898 ±1.7	0.9887 ±1.2	2.0620 ±0.0	0.9995 ±3.8	0.1730 ±2.6
Patient 7 (BRATS 2012)	GAC	0.5154 ±0.4	0.6069 ±0.4	5.3852 ±0.0	0.9963 ±2.7	26.4020 ±4.0
	LAC	0.6850 ±0.4	0.6436 ±0.2	4.9904 ±0.3	0.9975 ±7.0	14.1543 ±6.6
	ACCS	0.8995 ±1.2	0.9364 ±5.6	2.9634 ±2.3	0.9986 ±0.9	28.3751 ±5.9
	OSH-ACM	0.9789 ±1.5	0.9871 ±1.1	2.0458 ±0.0	0.9997 ±0.0	0.1356 ±1.8
Patient 8 (BRATS 2012)	GAC	0.5471 ±0.4	0.5565 ±0.3	5.8990 ±1.0	0.9904 ±0.5	24.9600 ±1.3
	LAC	0.7693 ±0.6	0.7895 ±0.5	4.3852 ±1.0	0.9985 ±2.8	16.8878 ±1.0
	ACCS	0.9599 ±0.6	0.9601 ±4.0	2.7945 ±0.0	0.9950 ±3.3	36.7810 ±1.8
	OSH-ACM	0.9886 ±2.4	0.9749 ±1.0	2.0827 ±1.1	0.9987 ±4.6	0.1321 ±3.6
Patient 9 (BRATS 2012)	GAC	0.6878 ±0.2	0.6558 ±0.0	5.0915 ±0.2	0.9967 ±0.0	15.7585 ±4.5
	LAC	0.8095 ±0.0	0.8947 ±0.1	3.1623 ±2.0	0.9974 ±7.7	8.5422 ±8.9
	ACCS	0.9097 ±3.0	0.8997 ±0.4	3.1597 ±5.3	0.9988 ±9.6	17.1467 ±2.4
	OSH-ACM	0.9877 ±1.4	0.9782 ±0.5	2.1284 ±0.0	0.9996 ±0.8	0.1879 ±0.3
Patient 10 (BRATS 2012)	GAC	0.5499 ±0.3	0.4998 ±0.1	6.7823 ±0.0	0.9945 ±9.1	20.8182 ±6.2
	LAC	0.6867 ±0.3	0.6577 ±0.1	5.1644 ±0.1	0.9959 ±2.2	8.0357 ±9.8
	ACCS	0.9002 ±4.2	0.9147 ±2.5	2.9846 ±7.3	0.9979 ±0.4	18.7666 ±0.0
	OSH-ACM	0.9868 ±1.0	0.9786 ±0.2	2.0628 ±1.0	0.9997 ±2.0	0.2429 ±4.7

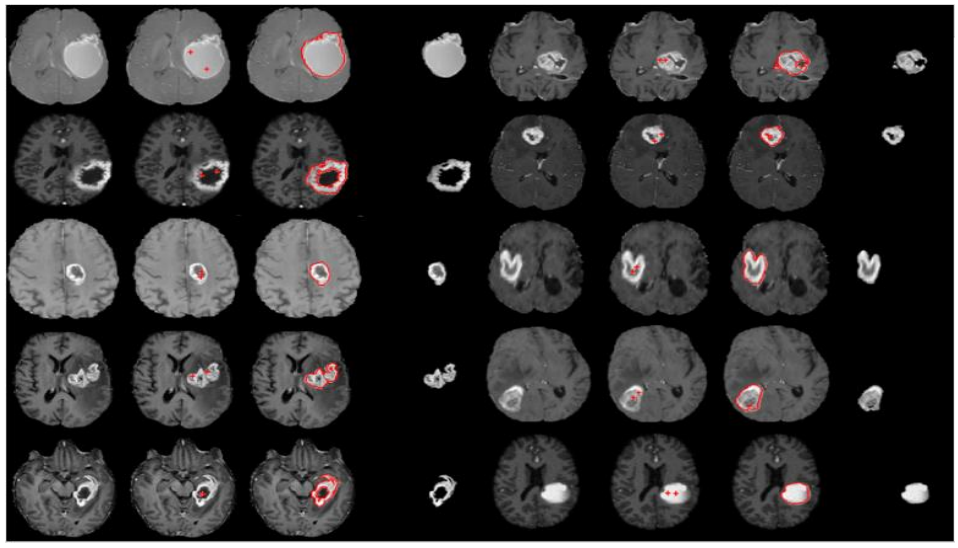

Figure 4: Segmentation Results by Our Method on BRATS 2012 and 2013 Databases.

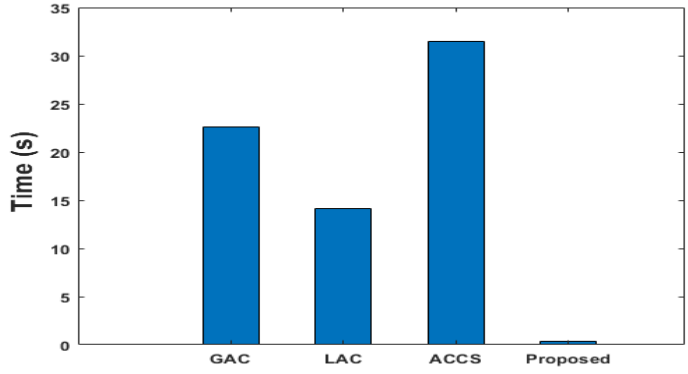

Figure 5: Comparison of the OSH method with state-of-the-art regarding computation time.

As illustrated in Figure 7, our method achieves a reduction in computation time compared to existing methods (expressed in seconds). The OSH method is faster compared to our previous approach because it recognizes the initial tumor contour in real time, which reduces the computational time required to evolve the active contour.

3.3 Evaluation of reconstruction phase

This new technique improves computational efficiency and pixel selection accuracy, which are essential for the reconstruction of 3D object shapes. The results of 3D object image reconstruction, based on real patients' dataset, are shown in table 3.

Table 3: 3D Segmentation results of real patient data from the BRATS 2019 database.

Patients	**Labels**	**Voxel count**	**Volume (mm^3)**	**Intensity Mean ±SD**
Patient 1	Clear Label	8 812 673	8.812673×10^6	32.4629 ± 76.7841
	Label with tumor	115 327	1.15327×10^5	434.7898 ± 75.9586
Patient 2	Clear Label	8 908 742	8.908742×10^6	31.0648 ± 66.3003
	Label with tumor	19 258	1.9258×10^4	424.8549 ± 65.4917
Patient 3	Clear Label	8 896 112	8.896112×10^6	24.4006 ± 649036
	Label with tumor	31 888	3.1888×10^4	451.9312 ± 57.2040
Patient 4	Clear Label	8 893 509	8.893509×10^6	36.5984 ± 90.5500
	Label with tumor	34 491	3.4491×10^4	1137.5650 ± 202.0132
Patient 5	Clear Label	8 874 450	8.874450×10^6	34.4983 ± 78.4227
	Label with tumor	53 550	5.3550×10^4	432.8664 ± 75.4400
Patient 6	Clear Label	8 815 463	8.815463×10^6	31.0447 ± 74.2778
	Label with tumor	112 537	1.12537×10^5	451.1814 ± 65.6239
Patient 7	Clear Label	8 800 705	8.800705×10^6	21.7560 ± 56.5531
	Label with tumor	127 295	1.27295×10^5	305.4569 ± 57.3601
Patient 8	Clear Label	8 872 783	8.872783×10^6	29.3676 ± 68.4357
	Label with tumor	55 217	5.5217×10^4	334.1023 ± 48.2186
Patient 9	Clear Label	8 920 644	8.920644×10^6	11.8151 ± 32.1527
	Label with tumor	7 356	7.356×10^3	198.0174 ± 38.5634
Patient 10	Clear Label	8 911 678	8.911678×10^6	23.9592 ± 59.2099
	Label with tumor	16 322	1.6322×10^4	454.6847 ± 83.4070
Patient 11	Clear Label	8 900 834	8.900834×10^6	35.1428 ± 75.6676
	Label with tumor	27 166	2.7166×10^4	344.4761 ± 46.2303

Patient 12	Clear Label	8 833 615	8.833615×10^6	64.3847 ± 39.4228
	Label with tumor	94 385	9.4385×10^4	580.9401 ± 36.3711
Patient 13	Clear Label	8 876 743	8.876743×10^6	68.8470 ± 153.2978
	Label with tumor	51 257	5.1257×10^4	698.3368 ± 120.9774
Patient 14	Clear Label	8 698 867	8.698867×10^6	25.9308 ± 57.5036
	Label with tumor	229 131	2.29131×10^5	304.6895 ± 70.7478
Patient 15	Clear Label	8 778 460	8.778460×10^6	44.1679 ± 112.9932
	Label with tumor	149 540	1.49540×10^5	442.8497 ± 45.4427
Patient 16	Clear Label	8 801 474	8.801474×10^6	18.6908 ± 43.6618
	Label with tumor	126 526	1.26526×10^5	241.1445 ± 36.7579
Patient 17	Clear Label	8 690 176	8.690176×10^6	16.6104 ± 39.7039
	Label with tumor	237 824	2.37824×10^5	213.0597 ± 45.3580
Patient 18	Clear Label	8 833 752	8.833852×10^6	16.8981 ± 43.7038
	Label with tumor	94 248	9.8248×10^4	270.6864 ± 44.3378
Patient 19	Clear Label	8 699 808	8.699808×10^6	16.7930 ± 41.8654
	Label with tumor	228 192	2.28192×10^5	227.5470 ± 37.6771
Patient 20	Clear Label	8 902 965	8.902965×10^6	47.3972 ± 115.0547
	Label with tumor	25 035	2.5035×10^4	477.4638 ± 28.0403

The data, in table 3, enable us to obtain the tumor volume for each patient with very respectable accuracy, making it easier to estimate the degree of cancer. These tables also provide useful information such as brain volume and mean intensity for each patient label (brain label and tumor label). The 3D reconstruction of the brain tumor is based on a given set of two-dimensional brain slices. The tumor areas of interest were extracted by the improved process of optical scanning holography (OSH) by extracting the maximum phase component, and the application, at the same time, of an active contour model (ACM) for faster segmentation of the region corresponding to the tumors in each slice. The results of this reconstruction are shown in figure 8 below.

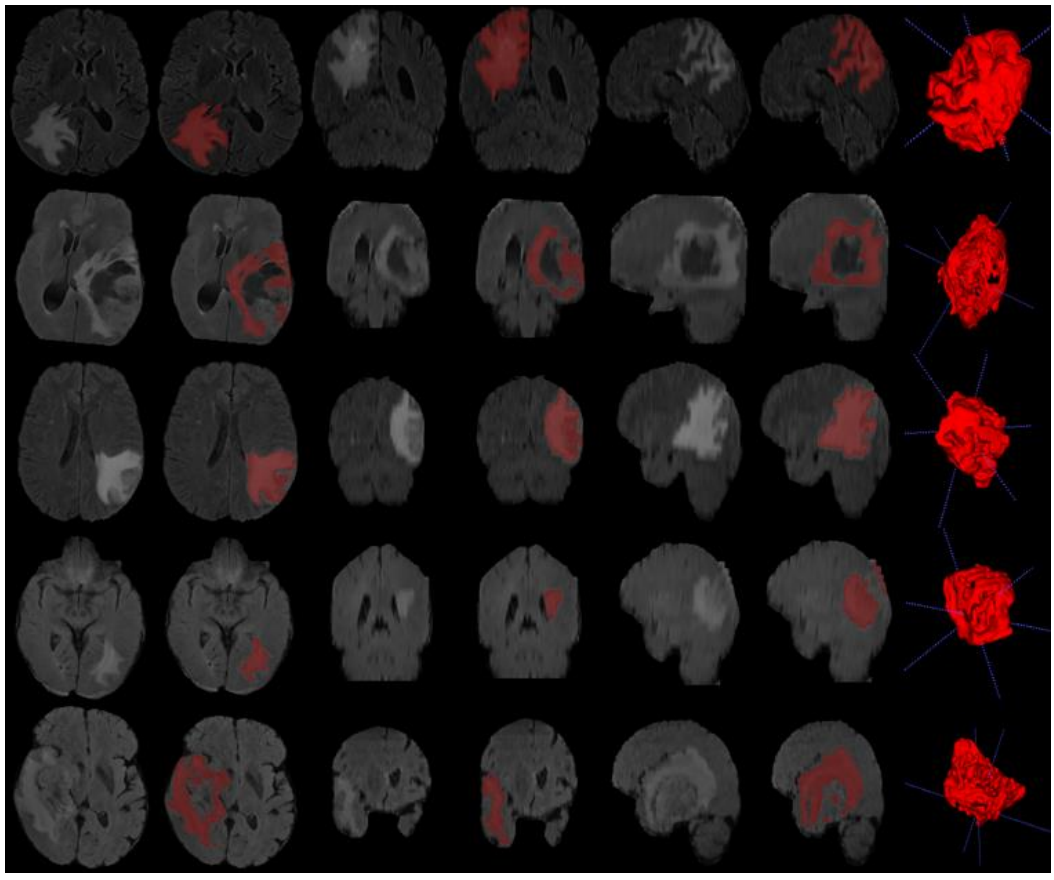

Figure 6: 3-D reconstruction results of real patient data from the MICCAI 2019-2020 databases.

4. CONCLUSION

In conclusion, this review underscores the significant advancements in our system for automating tumor tissue detection in MRI using Optical Scanning Holography (OSH). Our enhanced framework combines elements of in-line digital holography, a heterodyne fringe pattern, and the integration of an MR image display facilitated by a spatial light modulator (SLM). The result is a system that not only improves acquisition speed, accuracy, and data size but also introduces the concept of Generalized Optical Scanning Holography (GOSH), which allows the simultaneous acquisition of two on-axis holograms, reducing artifacts in reconstruction. This upgraded system takes advantage of line-by-line scanning with a cylindrical lens and leverages the precise collection of the outgoing phase component of the scanned current. This component reliably pinpoints the tumor's location, enabling faster and more accurate segmentation through an active contour model (ACM). The culmination of these advancements enables the reconstruction of 3D brain tumors from segmented regions of interest in each MRI slice. The continuous evolution of our system showcases its potential for significantly improving the efficiency and accuracy of tumor detection and segmentation in MRI,

offering promising prospects for the medical field and underscoring the potential of holographic technologies in medical imaging.

ACKNOWLEDGMENT

We would like to express our gratitude to the organizers of the Brain Tumor Segmentation (BraTS) challenge for providing us with the BRATS 2019 and 2020 databases. These datasets are instrumental in our research and contribute significantly to our work in the field of medical image analysis. Thank you for your valuable support [29-31].

REFERENCES

[1] The International Cancer Genome Consortium: "International network of cancer genome projects", Nature Vol 464/15 April 2010

[2] Ramin Ranjbarzadeh, Abbas Bagherian Kasgari, Saeid Jafarzadeh Ghoushchi, Shokofeh Anari, Maryam Naseri & Malika Bendechache: "Brain tumor segmentation based on deep learning and an attention mechanism using MRI multi-modalities brain images", Nature portfolio (2021)

[3] Megha P. Arakeri and G. Ram Mohana Reddy : "An Effective and Efficient Approach to 3D Reconstruction and Quantification of Brain Tumor on Magnetic Resonance Images", Medicine, Computer Science (2013)

[4] Matthias Bartels, Marius Priebe, Robin N Wilke, Sven P Kruger, Klaus Giewekemeyer, Sebastian Kalbfleisch, Christian Olendrowitz, Michael Sprung and Tim Salditt: "Low-dose three-dimensional hard x-ray imaging of bacterial cells", Optical Nanoscopy (Nov 2012)

[5] Kamlesh Pawar, Zhaolin Chen, N. Jon Shah, and Gary F. Egan : "An Ensemble of 2d Convolutional Neural Network for 3d Brain Tumor Segmentation", International MICCAI (2019)

[6] Kitara Kadhim Al-Shayeh, and Muzhir Shaban Al-Ani : "Efficient 3D Object Visualization via 2D Images", International Journal of Computer Science and Network Security, VOL.9 No.11, November 2009

[7] Qeethara Kadhim Al-Shayea and Muzhir Shaban Al-Ani : "An Efficient Approach to 3D Image Reconstruction", International Journal of Computer Science and Network Security, VOL.16 No.8, August 2016

[8] Hikmat Khan, Syed Farhan Alam Zaidi, Asad Safi, and Shahab Ud Din: 'A Comprehensive Analysis of MRI Based Brain Tumor Segmentation Using Conventional and Deep Learning Methods', International Symposium on Intelligent Computing Systems (March 2020)

[9] Wen-Wei Lin, Cheng Juang, Mei-Heng Yueh, Tsung-Ming Huang, Tiexiang Li, Sheng Wang, Shing-Tung Yau: "3D brain tumor segmentation using a two-stage optimal mass transport algorithm", Nature portfolio (2021)

[10] Pengyu Li, Wenhao Wu, Lanxiang Liu, Fardad Michael Serry, Jinjia Wang, Hui Han:" Automatic brain tumor segmentation from Multiparametric MRI based on cascaded 3D U-Net and 3D U-Net++", Biomedical Signal Processing and Control (Sep 2022)

[11] D. Gabor: "A new microscopic principle", Nature, 161 :777–778, 1948.

[12] U. Schnars and W. Jüptner: "Direct recording of holograms by a ccd target and numerical reconstruction", Applied optics, 33(2) :179–181, 1994.

[13] W. Xu, M.H. Jericho, I.A. Meinertzhagen, and H.J. Kreuzer: "Digital in-line holography for biological applications", Proceedings of the National Academy of Sciences, 98(20) :11301–11305, 2001.

[14] J. Garcia-Sucerquia, W. Xu, S.K. Jericho, P. Klages, M.H. Jericho, and H.J. Kreuzer: "Digital in-line holographic microscopy", Applied optics, 45(5) :836–850, 2006.
[15] E. Cuche, F. Bevilacqua, and C. Depeursinge: "Digital holography for quantitative phase-contrast imaging", Optics letters, 24(5) :291–293, 1999.
[16] B. Rappaz, P. Marquet, E. Cuche, Y. Emery, C. Depeursinge, and P.J. Magistretti: "Measurement of the integral refractive index and dynamic cell morphometry of living cells with digital holographic microscopy", Optics express, 13(23) :9361–9373, 2005.
[17] B. Kemper and G. von Bally: "Digital holographic microscopy for live cell applications and technical inspection", Applied optics, 47(4) :A52–A61, 2008.
[18] N. Demoli, D. Vukicevic, and M. Torzynski: "Dynamic digital holographic interferometry with three wavelengths", Optics Express, 11(7) :767–774, 2003.
[19] J. Zhao, H. Jiang, and J. Di: "Recording and reconstruction of a color holographic image by using digital lensless fourier transform holography", Optics express, 16(4) :2514–2519, 2008.
[20] P. Tankam, P. Picart, D. Mounier, J.-M. Desse, and J.C. Li: "Method of digital holographic recording and reconstruction using a stacked color image sensor", Applied optics, 49(3) :320–328, 2010.
[21] F. Charrière, J. Kühn, T. Colomb, F. Montfort, E. Cuche, Y. Emery,K. Weible, P. Marquet, and C. Depeursinge: "Characterization of microlenses by digital holographic microscopy", Applied Optics, 45(5) :829–835, 2006.
[22] J.-M. Desse, P. Picart, and P. Tankam: "Digital three-color holographic interferometry for flow analysis", Optics express, 16(8) :5471–5480, 2008.
[23] P. Tankam, Q. Song, M. Karray, J.-C. Li, J.-M. Desse, and P. Picart: "Real-time three-sensitivity measurements based on three-color digital fresnel holographic interferometry", Optics letters, 35(12) :2055–2057, 2010.
[24] K. Kim, H. Yoon, M. Diez-Silva, M. Dao, R.R. Dasari, and YK. Park: "High resolution three-dimensional imaging of red blood cells parasitized by plasmodium falciparum and in situ hemozoin crystals using optical diffraction tomography", Journal of biomedical optics, 19(1), 2013.
[25] F. Yaras, H. Kang, and L. Onural. Real-time phase-only color holographic video display system using led illumination. Applied optics, 48(34) :H48–H53,2009.
[26] P.-A. Blanche, A. Bablumian, R. Voorakaranam, C. Christenson, W. Lin, T. Gu, D. Flores, P. Wang, W.-Y. Hsieh, M. Kathaperumal, B. Rachwal, O. Siddiqui, J. Thomas, R.A. Norwood, M. Yamamoto, and N. Peyghambarian. Holographic three-dimensional telepresence using large-area photorefractive polymer. Nature, 468 :80–83, 2010.
[27] J. Geng. Three-dimensional display technologies. Advances in optics and photonics, 5(4) :456–535, 2013.
[28] M. Kujawinska, T. Kozacki, C. Falldorf, T. Meeser, B.M. Hennelly, P. Garbat, W. Zaperty, M. Niemelä, G. Finke, M. Kowiel, and T. Naughton. Multiwavefront digital holographic television. Optics express, 22(3):2324–2336, 2014.
[29] H. Mukawa: "A full color eyewear display using holographic planar waveguides", SID Dig., pages 89–92, 2008.
[30] C. Jang, C.-K. Lee, J. Jeong, G. Li, S. Lee, J. Yeom, K. Hong, and B. Lee: "Recent progress in see-through three-dimensional displays using holographic optical elements", Applied optics, 55(3) :A71–A85, 2016.
[31] I. Yamaguchi and T. Zhang: "Phase-shifting digital holography", Optics letters, 22(16) :1268–1270, 1997.
[32] I. Yamaguchi, J. Kato, S. Ohta, and J. Mizuno: "Image formation in phaseshifting digital holography and applications to microscopy", Applied Optics, 40(34) :6177–6186, 2001.

[33] F. Le Clerc, L. Collot, and M. Gross. Numerical heterodyne holography with two-dimensional photodetector arrays. Optics letters, 25(10) :716–718, 2000.

[34] E. Absil, G. Tessier, M. Gross, M. Atlan, N. Warnasooriya, S. Suck, M. Coppey-Moisan, and D. Fournier. Photothermal heterodyne holography of gold nanoparticles. Optics Express, 18 :780–786, 2010.

[35] B. Samson, F. Verpillat, M. Gross, and M. Atlan. Video-rate laser Doppler vibrometry by heterodyne holography. Optics letters, 36(8) :1449–1451, 2011.

[36] T.-C. Poon: "Three-dimensional image processing and optical scanning holography", Advances Imaging & Electron Physics 126, 329-350 (2003).

[37] Bradley W. Schilling and Ting-Chung Poon, "Real-time preprocessing of holographic information," Opt. Eng.,vol. 34, no. 11, pp. 3174–3180, Nov 1995.

[38] Guy Indebetouw, Wenwei Zhong, and David Chamberlin-Long, "Point-spread function synthesis in scanning holographic microscopy," J. Opt. Soc.Am. A, vol. 23, no. 7, pp. 1708–1717, Jul 2006.

[39] Xin Zhang and Edmund Y. Lam: "edge detection of three-dimensional objects by manipulating pupil functions in an optical scanning holography system", Proceedings of 2010 IEEE 17th International Conference on Image Processing

[40] Momonoi Y, Taira K, Hirayama Y, "Scan-type image capturing system using a cylindrical lens for one dimensional integral imaging", International Society for Optics and Photonics, 6490 649017 (2007).

[41] Essadike, Abdelaziz, Elhoussaine Ouabida, and Abdenbi Bouzid. "Optical scanning holography for tumor extraction from brain magnetic resonance images." Optics Laser Technology 127 (2020): 106158.

[42] Abdelaziz, Essadike, et al. "Optical based approach for brain tumor segmentation." 2020 1st International Conference on Innovative Research in Applied Science, Engineering and Technology (IRASET). IEEE, 2020.

[43] Ouabida, Elhoussaine, Abdelaziz Essadike, and Abdenbi Bouzid. "Optical correlator based algorithm for driver drowsiness detection." Optik 204 (2020): 164102.

[44] Essadike, Abdelaziz, Elhoussaine Ouabida, and Abdenbi Bouzid. "Brain tumor segmentation with Vander Lugt correlator based active contour." Computer methods and programs in biomedicine 160 (2018): 103-117.

[45] Ouabida, Elhoussaine, Abdelaziz Essadike, and Abdenbi Bouzid. "Automated segmentation of ophthalmological images by an optical based approach for early detection of eye tumor growing." Physica Medica 48 (2018): 37-46.

[46] Ouabida, Elhoussaine, Abdelaziz Essadique, and Abdenbi Bouzid. "Vander Lugt Correlator based active contours for iris segmentation and tracking." Expert Systems with Applications 71 (2017): 383-395.

[47] Cherkaoui, A., El-Ouarzadi, A., Essadike, A., & Bouzid, A., Automatic Brain Tumor Detection and Segmentation Using Enhanced Optical Scanning Holography and Active Contour Model in MRI. Sensors & Transducers, 2023 ; 262(2), 13-22.

[48] Abdelaziz Essadike, Elhoussaine Ouabida, Abdenbi Bouzid. Medical Image Segmentation by Active Contour Improvement. American Journal of Software Engineering and Applications. Vol. 6, No. 2, 2017, pp. 13-17. doi: 10.11648/j.ajsea.20170602.11

[49]. Iv_an Cabria and Iker Gondra. Mri segmentation fusion for brain tumor detection. Information Fusion, 36:1-9, 2017.

[50]. Vicent Caselles, Ron Kimmel, and Guillermo Sapiro. Geodesic active contours. International journal of computer vision, 22(1):61-79, 1997.

[51]. Elisee Ilunga-Mbuyamba, Juan Gabriel Avina-Cervantes, Arturo Garcia-Perez, Rene de Jesus Romero-Troncoso, Hugo Aguirre-Ramos, Ivan Cruz-Aceves, and Claire Chalopin. Localized active contour model with background intensity compensation applied on automatic mr brain tumor segmentation. Neurocomputing, 220:84-97, 2017.

[52]. Elisee Ilunga-Mbuyamba, Jorge Mario Cruz-Duarte, Juan Gabriel Avina-Cervantes, Carlos Rodrigo Correa-Cely, Dirk Lindner, and Claire Chalopin. Active contours driven by cuckoo search strategy for brain tumour images segmentation. Expert Systems with Applications, 56:59-68, 2016.